Nanoscale

PAPER

Check for updates

Sustainable carbon dot-based fluorosensor integrated with a microcontroller-driven portable device for on-site nanomolar detection of picric acid

Mallika Phull, [ID] [a] Amjad Ali, [ID] [a] Jobanpreet Brar,[b] Amit Mishra[b] and Banibrata Maity [ID] *[a]

This study reports the development of a microcontroller-based, portable fluorometric sensing device for the rapid and highly sensitive detection of picric acid (PA), a hazardous nitroaromatic explosive. The sensor utilizes biomass-derived carbon dots synthesized from watermelon extract (*Citrullus lanatus*) *via* a sustainable, hydrothermal green synthesis route, free of toxic reagents or additives. The resulting water-soluble carbon dots (W-CDs) exhibit strong cyan fluorescence under UV light with a high quantum yield of 29%. Comprehensive characterizations using FTIR, XRD, HRTEM, Raman, XPS, UV-Vis, steady-state, and time-resolved fluorescence spectroscopy, confirmed their structural, morphological, and optical properties. These W-CDs serve as an effective "turn-off" fluorescent probe for PA, achieving an ultra-low detection limit of 4.17 nM in aqueous solution. The integration of W-CDs into a portable device enables real-time, on-site detection, with results closely matching standard laboratory measurements. Selectivity studies confirmed minimal interference from other analytes in complex samples. Additionally, an AND logic gate was implemented using the fluorescence response, highlighting the system's potential for intelligent chemical sensing. This work demonstrates the integration of eco-friendly nanomaterial synthesis with low-cost device engineering, offering a practical platform for environmental monitoring and explosive detection.

1. Introduction

Nitroaromatics are widely employed in the production of explosives, dyes, insecticides, and medicines, and are also essential in forensic and military contexts.[1] Extended testing, storage, and disposal of nitroaromatics result in river pollution, soil degradation, and ecological disruption, culminating in substantial environmental damage.[2] Several well-known nitro explosive substances include 2,4,6-trinitrotoluene (TNT), 2,4-dinitrotoluene (DNT), and 2,4,6-trinitrophenol (TNP).[3] Among these, 2,4,6-trinitrophenol (TNP), commonly referred to as picric acid (PA) is notable as the most significant nitroaromatic compound because of its environmental effects and role as an intermediate in explosives manufacturing.[4] Presence of nitro and phenolic functionalities, makes TNP poorly bio-

degradable, toxic and explosive. Besides this, TNP poses severe health risks, such as anemia, skin irritation, respiratory damage from inhalation, liver dysfunction and can be absorbed through the skin as well. Recognized as both an environmental contaminant and human carcinogen, TNP presents significant health and ecological concerns.[5] So, detection of these explosives has become a critical task, owing to their widespread use in public safety measures, national defense, and security operations.[6] Till now, reported methods for both qualitative as well as quantitative analysis of nitroaromatics include Raman spectroscopy,[7] high performance liquid chromatography,[8,9] gas chromatography,[8] electrochemical techniques[10,11] and mass spectrometry.[12] However, all these techniques rely on high priced instruments and are less sensitive, hugely limiting their practical utility.[13] Given these odds, a more effective approach is employing fluorescence spectroscopy, which is straightforward and very sensitive technique. Fluorescent-based probes provide various benefits, such as quick response and smooth functioning.[14] Several literature reports have demonstrated the use of polymer-based and supramolecular probes for the sensing of picric acid (PA), owing to their structural versatility and selective host–guest

[a]Department of Chemistry and Biochemistry, Thapar Institute of Engineering and Technology, Patiala, 147004, India. E-mail: phullmallika96@gmail.com, amjadali@thapar.edu, banibrata.maity@thapar.edu
[b]Department of Electronics and Communication Engineering, Thapar Institute of Engineering and Technology, Patiala, 147004, India.
E-mail: jbrar2_be21@thapar.edu, amit_mishra@thapar.edu

interactions.[15,16] However, these systems often suffer from limitations such as complex synthesis, poor aqueous solubility, lower biocompatibility, and limited scalability. In contrast, carbon-based nanomaterials like carbon dots offer significant advantages, including facile green synthesis, excellent water dispersibility, high stability, and tunable fluorescence, making them more suitable for practical and environmentally friendly sensing applications.[17,18] Interestingly, on combining these explosives with carbon-based nanomaterials, fluorescence of carbon-based nanomaterials gets quenched, making the presence of explosives detectable.[19] Zero-dimensional nanomaterials, such as carbon dots (CDs), are spherical shaped generally sized less than 10 nm, consisting of sp^2- and sp^3-hybridized carbon frameworks.[20] Their exceptional photostability, low toxicity, eco-friendliness, adjustable photoluminescence properties, high water solubility, and excellent biocompatibility make them appropriate for diverse applications, including sensing, biomedicine, drug delivery, optoelectronics, catalysis, biological imaging, and photocatalysis.[21,22] The fluorescence characteristics of CDs can be efficiently modified through precursor design, surface passivation, and optimization of reaction conditions, making them highly versatile for many applications.[23,24] CDs can be synthesized using top-down (e.g., laser ablation, electrochemical oxidation, arc-discharge) or bottom-up (e.g., ultrasonic, microwave, hydrothermal, solvothermal) approaches.[25] However, top-down methods often involve complex processes, high costs, and time-intensive procedures, whereas bottom-up techniques are simpler and more environmentally friendly.[26] CDs are often derived from organic compounds or biomass precursors, but the toxicity and high cost of aromatic sources limit their use.[27] Biomass offers a sustainable and eco-friendly source of carbon, enabling the synthesis of nanomaterials through green and cost-effective methods. Its natural abundance and rich carbon content make it ideal for producing carbon-based sensors with minimal environmental impact.[28] As a result, biomass-derived CDs are favored for their cost-effectiveness and sustainability, naturally incorporating heteroatoms that enhance their properties without requiring further modification.[29]

Watermelon juice primarily consists of 90–92% water, natural sugars (fructose, glucose, sucrose), vitamins (C, A, B6), minerals (potassium, magnesium), and bioactive compounds like lycopene and citrulline, making it a hydrating and nutrient-rich beverage. Additionally, watermelons are abundant in polysaccharides, amino acids, vitamins, and trace elements.[30] Therefore, we selected watermelon peels as a precursor for synthesizing carbon dots (CDs) via the hydrothermal method, ensuring an eco-friendly approach by avoiding toxic solvents and reducing preparation costs.

Zong et al. synthesized CDs by utilizing coffee residues as a biomass-based precursor for detection for PA with a limit of detection (LOD) of 0.26 μM.[31] Yang et al. fabricated CDs derived from edible soy sauce with 5.7% quantum yield.[32] This as-prepared nanoprobe system was then used for selective detection of PA with the LOD of 70 nM. Kalanidhi et al. syn-

thesized CDs using a facile hydrothermal process from betel leaf, additionally using NH_3 solution as source of N-dopant. The developed system was employed for detection of PA with LOD of 3.3 μM.[33] Li et al. used grape skin as green precursor for synthesizing CDs with 18.67% quantum yield and further used it for detection of PA with LOD 79.4 μM.[34] Poddar et al. synthesised carbon dots by utilising discarded glycerol obtained from biodiesel production and employed it as fluorescent sensor for detection of PA with 1.07 μM LOD.[35] Britto et al. used mushroom as a carbon precursor and synthesised carbon dots using one step hydrothermal approach. The developed probe was used for selective detection of PA with 2% quantum yield and high LOD in nanomolar range.[36] Koparde et al. synthesised fluorescent carbon dots by using kitchen waste okra peels by pyrolysis combined with reflux method. The as prepared nanoprobe was used for detection of metal ions as well as nitroaromatic compound, PA with a LOD of 2.10 μg mL^{-1} and 12% quantum yield.[37]

Spectroscopy-based methods, including optical sensors, offer high sensitivity and reliability, but their equipment-heavy nature and sophisticated instrumentation can limit portability for real-time applications. This highlights the need for developing compact and portable sensing platforms that retain analytical performance while enabling on-site detection. A single spectroscopy sensor can perform efficiently over multiple spectral ranges such as visible (VIS), ultraviolet (UV), and infrared (IR) regions.[38,39] Recent advancements in spectrophotometry have resulted in simple, self-made spectrophotometers.[40,41] These sensor systems are often characterized by a 3D-printed or cardboard enclosure with a specific compartment for sample insertion, where light is transmitted through a cuvette for spectral measurement. The development of commodity Internet of Things (IoT) based optical sensors is making it easy to integrate spectroscopy sensor systems seamlessly, making them more accessible for simple, practical, and easily deployable spectroscopy applications.[42,43]

The pressing necessity to achieve safety and environmental sustainability compels the innovation of low-cost, portable spectroscopy sensor-based electronic devices for the detection of nitroaromatics such as PA in industrial waste and military discards from cantonment regions. Traditional detection techniques usually involve complex laboratory setups, hence time-consuming, expensive, and less accessible, particularly in resource-constrained areas. The creation of low-cost, portable spectroscopy sensor-based electronic devices has the potential to revolutionize nitroaromatics monitoring by allowing rapid and accurate on-site detection of explosives such as PA. These cost-effective interventions would enable communities, regulators, and the environment agencies to perform real-time audits, recognize hotspots, and implement early corrective actions and therefore minimize the detrimental impacts of nitroaromatic pollution and ensure the safety of individuals along with the environment. In contrast to previously reported smartphone-based paper devices that rely on external UV sources and image-based fluorescence analysis, yielding only

pixel-based estimates and semi-quantitative results,[44–46] our work introduces an advanced microcontroller-based portable fluorometric system that enables real-time spectral acquisition, wavelength tuning, and quantitative fluorescence measurement, delivering performance comparable to that of a standard spectrofluorometer.

This work represents a significant technological advancement through the green synthesis of highly fluorescent carbon dots (W-CDs) from watermelon extract, achieved without any toxic reagents, thus supporting sustainable nanomaterial development (UN SDG 12). The W-CDs exhibit a remarkable quantum yield of 29%, enabling highly sensitive detection of picric acid with a low detection limit of 4.17 nM. Moreover, the development of a self-contained, microcontroller-based portable fluorometric device marks a major step forward, delivering selectivity, sensitivity, and stability comparable to a standard spectrofluorometer while ensuring on-site applicability. Furthermore, logic gate functionality was incorporated into the system, where the fluorescence response of the probe to different analytes was used to perform Boolean operations. This approach enabled the creation of fundamental logic operations, such as the AND gate, by analyzing the spectral variations of W-CDs in the presence of PA. Interference studies were conducted to assess the impact of other substances on the detection process, confirming the high sensing efficiency and selectivity of the portable sensor system for detection of PA.

2. Materials and method

Watermelon (*Citrullus lanatus*) extract was purchased additive free from a local market, in Patiala, Punjab, India. Chemicals such as $Hg(NO_3)_2$, $CrCl_3$, $PbCl_2$, $Na_2HAsO_4 \cdot 7H_2O$, $NaAsO_2$, 2,4-dinitrotoluene (2,4-DNT), 2-nitrophenol (2-NP), 3-nitrophenol (3-NP), 4-hydroxybenzaldehyde, quercitine, resorcinol, catechol, hydroquinone, picric acid, 2-nitrobenzaldehyde, 3-nitroaniline, 4-nitrobenzaldehyde, nitrobenzene and phenol, NaCl, HCl and NaOH were procured from Loba Chemie Pvt. Ltd, India. Ultrapure deionized water was used for preparing stock solutions of all analytes and were used as such without further purification.

2.1. Synthesis of W-CDs

Preservative-free watermelon juice was refrigerated for 6 hours and sonicated (Ultrasonic cleaner, Labman Scientific Instruments) for 30 min. After this, 25 mL of juice was transferred to a Teflon-lined autoclave and was subjected to hydrothermal pyrolysis at 150 °C for 3 h. The reaction was accompanied by a color change from red to dark brown, which indicated the formation of carbon dots. Furthermore, the resulting liquid was centrifuged (REMI C-30 Plus) at 10 000 rpm for 10 min over 3 cycles to separate unreacted residue and large-sized particles. The obtained supernatant was further purified by syringe filtration using 0.22 μm and subsequently underwent dialysis for 72 hours using HI-MEDIA 110 LA395-1MT dialysis membrane as shown in Scheme 1. The purified solution was stored at 3 °C in the refrigerator as stock solution and was labeled as W-CDs. To ensure consistency and reliability of results, a fresh batch of W-CDs was synthesized prior to each experimental procedure.

2.2. Instrumentation

UV-vis spectrophotometer (Shimadzu UV-2450) was used to record the absorption spectra of W-CDs. Functional group analysis was performed with a Shimadzu IRTracer-100 Fourier transform infrared (FTIR) spectrophotometer. Fluorescence emission spectra and lifetime decay were measured using a Shimadzu RF-600 and a Delta-Flex modular fluorescence life-
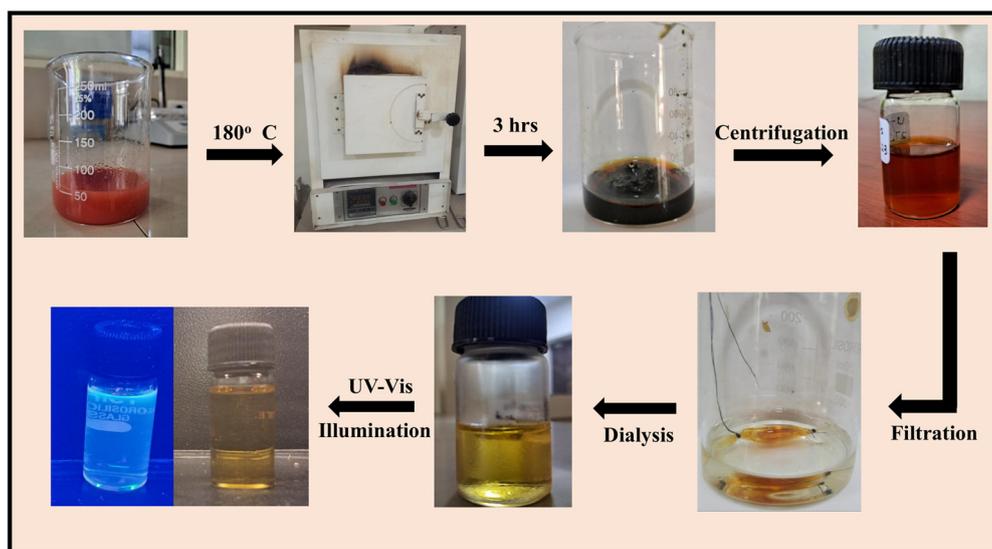
Scheme 1 Sustainable synthesis of W-CDs from watermelon (*Citrullus lanatus*) extract.

time spectrofluorimeter (HORIBA Scientific), with an instrument response function (IRF) of ~200 ps and a 300 nm nanoLED excitation source. Fluorescence emission spectra and lifetime decay were recorded on (Shimadzu RF-600) and Delta-Flex modular fluorescence lifetime spectrofluorimeter (HORIBA Scientific) with IRF (Instrument response function) ~200 ps and 300 nm (nanoLED) excitation source. The elemental composition of the W-CDs was analyzed using X-ray photoelectron spectroscopy (XPS) PHI 5000 Versa Probe III. The particle size and morphology were confirmed by high-resolution transmission electron microscopy (HRTEM) using a JEOL JEM 2100 Plus. Surface defects were characterized with a Raman spectrometer (LabRAM HR Evolution) employing a 532 nm laser radiation source. The amorphous structure of the W-CDs was examined by X-ray diffraction (XRD) using Rigaku Smart LAB SE diffractometer with Cu Kα radiation ($\lambda = 1.540$ Å).

2.3. Measurement of photoluminescence quantum yield (PLQY)

The PLQY of W-CDs and in presence of picric acid (PA) was calculated by using quinine sulphate as reference ($\phi = 0.546$), given by the equation:

$$\phi_S = \phi_R \times \frac{A_S}{A_R} \times \frac{(\text{Abs})_R}{(\text{Abs})_S} \times \frac{\eta_S^2}{\eta_R^2} \qquad (1)$$

where symbol 'ϕ' represents PLQY, 'A' and 'Abs' represents area under curve of PL emission spectra and absorbance recorded at 340 nm wavelength and subscripts 'R' and 'S' corresponds to reference and sample (W-CDs) respectively. PLQY was evaluated in three independent trials.

2.4. Outline of experimental procedure

In a 3.5 mL cuvette, 2 mL of distilled water and 20 μL of W-CDs stock solution were added and thoroughly mixed by retro pipetting to achieve a homogeneous solution. The excitation wavelength was optimized at 340 nm, and the emission spectra were recorded over the range of 350 nm to 600 nm with a scan rate of 2000 nm min^{-1}. Additionally, volume of W-CDs and the slit width were also optimized, with 20 μL of W-CDs and a slit width of 5/10 nm yielding the highest PL intensity, Fig. S1a and S1b. These optimizations were carried out with an aim to achieve a narrower peak and good spectral resolution. These experimental parameters were maintained consistently throughout, and all measurements were recorded in triplicate to ensure reproducibility. Additionally, to assess the selectivity of different analytes towards as-prepared probe W-CDs, 100 μL of 1 mM stock solution of each analyte was added.

3. Findings and analysis

3.1. Characterizations of W-CDs

The Raman spectrum was recorded in order to decipher the structural properties of the as -prepared W-CDs, as shown in Fig. 1a. It depicted two well-defined peaks at 1352 cm^{-1} and 1598 cm^{-1} attributing to disordered-D band and graphite-G band respectively. D-Band indicated presence of defects associated with sp^3 carbon atoms due to breathing motion of κ-phonons with A$_{1g}$ symmetry mode. Strong D-band corresponded to higher degree of disorder. Similarly, graphite band appeared due to first order scattering of E$_{2g}$ phonons by sp^2 hybridised carbon atoms, highlighting graphitic domains in W-CDs.[47] A sharp G-band indicated high degree of graphitisation. Additionally, intensity ratios corresponding to D and G band, $I_D : I_G$ band were computed to be 0.92, which outlined large number of defects and graphitisation.[48]

Fourier transform infrared spectroscopy (FTIR) was employed to account for the presence of different functional groups on the surface of the W-CDs, as depicted in Fig. 1b. A broad absorption band observed at 3399 cm^{-1} is attributed to –O–H stretching vibration. Another sharp peak at 1625 cm^{-1} correspond to C=C stretching, set of minor yet significant peaks at 1304, 1191 and 1134 cm^{-1} ascribed to C–O stretching, C–C stretching and C–H in plane bending in aromatic hydrocarbons respectively.[49,50] FTIR analysis revealed the abundance of hydrophilic functional groups on W-CQDs, supporting its water solubility.[51] Fig. 1c exhibits X-Ray diffraction pattern of W-CDs which showed a prominent diffraction peak centred at 23.3° corresponding to (002) graphitic carbon (sp^2 C) lattice place, demonstrating amorphous nature of W-CDs.[29,49] Besides this, high resolution transmission electron microscopy (HR-TEM) was used to examine the size and morphology of the synthesized W-CDs as shown in Fig. 1d and Fig. S1c, S1d. The particles exhibited a nearly spherical shape with good monodispersity and the inset of Fig. 1d presents a particle size distribution histogram ranging from 2 to 12 nm, with an average particle size of 7.20 ± 2.06 nm.

Furthermore, XPS analysis was executed to investigate the elemental surface composition of as prepared W-CDs. Fig. 2a depicts survey spectrum showing two spiked peaks at 283.8 eV attributing to C 1s (72.22%) and 529.3 eV to O 1s (27.78%) respectively. On deconvolution, high resolution C 1s spectra revealed three peaks at 284.7, 286.2 and 288.1 eV, corresponding to C–C/C=C, C–OH and O=C–O respectively (Fig. 2b).[49,52] Analogously, O 1s (Fig. 2c) indicated major peaks at 531.6, 532.2, 533.4 eV ascribing to C=O, C–O–C/C–OH and H–OH, in order.[53] Dynamic light scattering (DLS) was executed to evaluate the hydrodynamic particle size. An average particle size of 59 nm was observed in three cycles, Fig. 2d. The larger particle size observed in DLS can be attributed to the formation of an electrical double layer and the path hindrance caused by overlapping nanoparticles.[54]

3.2. Deciphering optical properties

The optical properties of W-CDs were explored by using UV-vis absorption spectra and fluorescence emission spectra. Fig. 3a outlined two significant peaks at 223 and 283 nm corresponding to π–π* and n–π* transitions due to sp^2 carbon domains and carbonyl group (C=O) of W-CDs.[55] The as-prepared W-CDs appeared pale brown under visible light and emitted cyan fluorescence when exposed to UV irradiation at 365 nm, as shown in the inset (Fig. 3a). This observation is
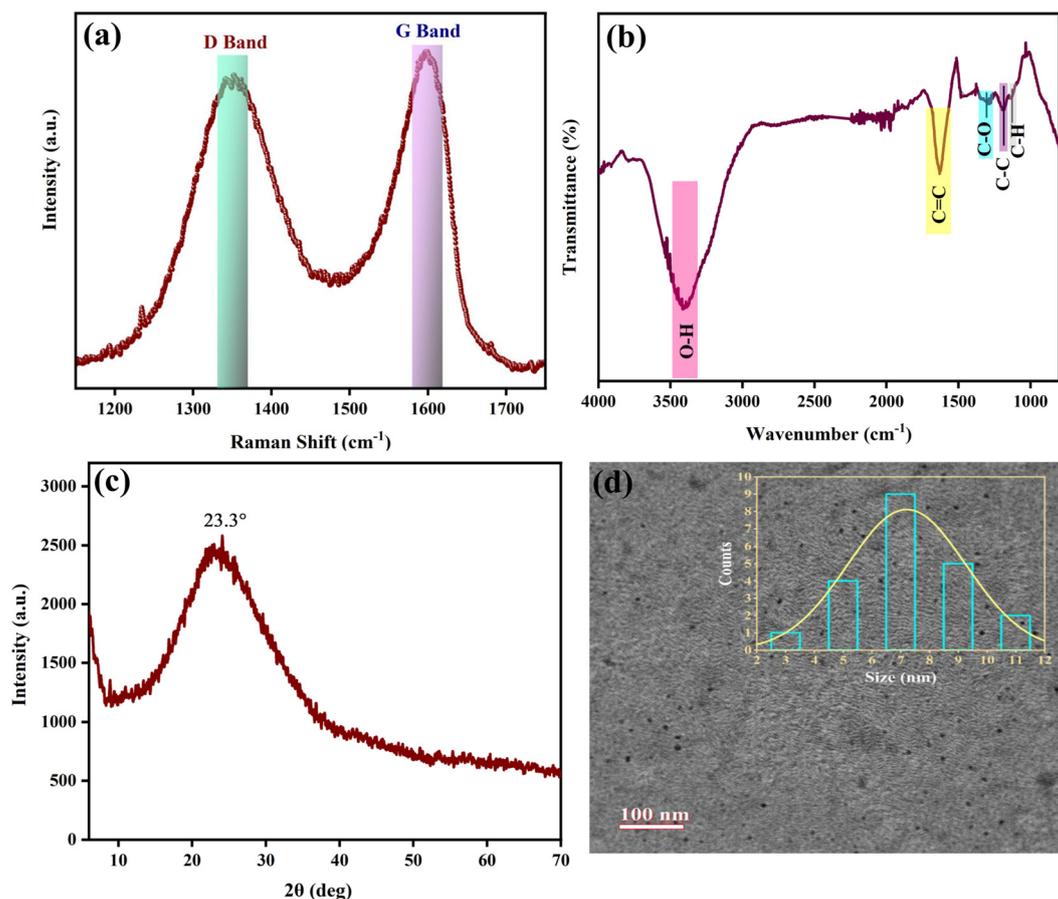
Fig. 1 (a) Raman spectrum, (b) FTIR spectrum, (c) XRD of W-CDs and (d) HR-TEM image of W-CDs at 100 nm resolution with inset showing particle size distribution histogram plot.

ascertained to the radiative recombination between electrons and holes, resulting from photoinduced charge separation and surface site trapping, ultimately leading to photoluminescence (PL) emission of W-CDs.[29,56] The fluorescence properties of synthesized CDs were investigated by recording the excitation and emission spectra, as depicted in Fig. 3b. The emission maxima was obtained at 432 nm, upon excitation at 340 nm. The PLQY of W-CDs was calculated by using eqn (1) and was found to be 29% (Table S1). W-CDs demonstrated characteristic excitation-dependent fluorescence behavior, as evident from the 3D spectra obtained in aqueous solution, Fig. 3c.[57] Fluorescence emission spectra at various excitation wavelengths were recorded and analyzed, as depicted in Fig. S2a. The emission wavelengths exhibited a huge bathochromic shift of 116 nm as the excitation wavelength of W-CDs was varied from 290 to 490 nm, Fig. 3d. This observation of excitation dependent emission can be attributed to various factors namely zig zag sites, sp^2 domains, surface defects, and quantum confinement effect.[58]

3.3. Stability evaluation

Evaluating the stability of W-CDs is a critical step to ensure the reliability of fabricated nanoprobe for advanced fluorescence-

based sensing applications. Therefore, effect of pH, photoirradiation and ionic strength experiments were thoroughly examined. In addition, W-CDs had an intrinsic pH of 3.9 as shown in Fig. S2b, which indicates its acidic nature. This finding was consistent with the zeta potential −8.45 mV indicating the presence of negatively charged groups on the surface of W-CDs, Fig. S3a.[59] A shift from acidic pH to neutral pH (7) led to an enhancement in PL emission. However, in alkaline pH, significant drop in PL intensity was noted. This reduction may be associated with the deprotonation of carboxylate and ammonium groups, thereby increasing the accumulation of negative charge. As a result, energy levels become occupied, disrupting electronic transitions at emissive traps. This disturbance led to a decrease in PL emission coupled with a bathochromic shift in the emission spectrum.[60] The maximum PL intensity noted in neutral pH, can be ascribed to the formation of zwitterionic species due to interactions between hydroxyl and carboxylic acid present on the surface of W-CDs (verified by FTIR and XPS analyses).[61] Thus, the proposed nano sensor shows potential for advanced applications in neutral aqueous medium. The photostability of W-CDs was evaluated by irradiating to a Xe-arc lamp for a duration of 100 minutes, shown in Fig. S2c during which no considerable change in intensity
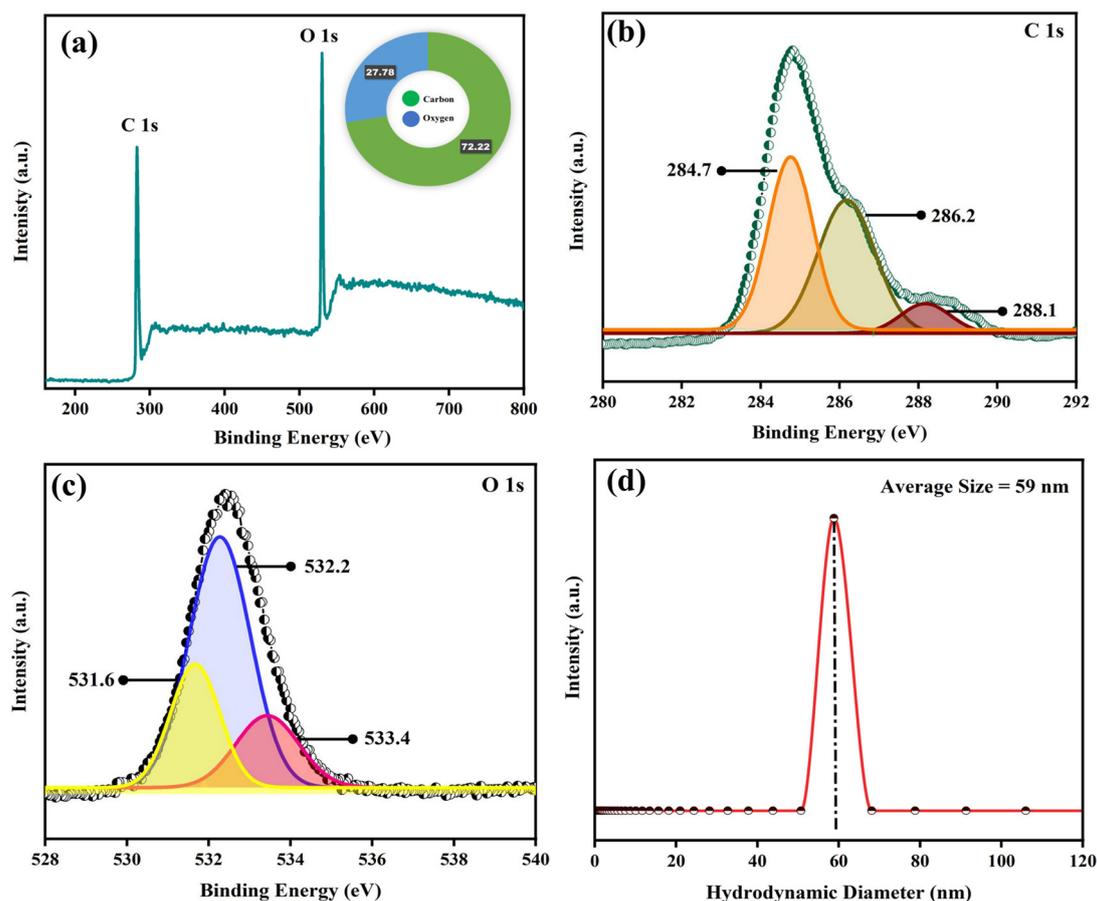
Fig. 2 (a) High-resolution XPS survey spectrum, (b) deconvoluted C 1s spectrum, (c) deconvoluted O 1s spectrum of W-CDs and (d) DLS analysis of W-CDs.

was observed indicating good photobleaching property.[29] Fig. S2d shows the impact of ionic strength on PL of W-CDs in presence of different concentration of NaCl salt. There were no significant changes in PL intensity or emission maxima of W-CDs at various ionic strengths, thereby highlighting the excellent stability of nanoprobe in saline environments. All these studies confirmed the stability of as-prepared W-CDs and their potential for sensing applications.

3.4. Selectivity studies

The selectivity of fabricated nanosensor, was investigated by monitoring the changes in PL intensity of W-CDs upon interaction with various divalent and trivalent metal ions such as As^{3+}, As^{5+}, Cr^{2+}, Hg^{2+}, Ni^{2+}, Pb^{2+}, Cu^{2+}, Fe^{3+}, and Fe^{2+} and organic analytes like 2,4-DNT, 2-NP, 3-NP, 4-hydroxybenzene, quercetin, resorcinol, catechol, hydroquinone, PA, 2-nitrobenzaldehyde, 3-nitroaniline, 4-nitrobenzaldehyde, nitrobenzene, and phenol, as shown in Fig. 4a and b respectively. For the analysis study, 1 mM stock solutions of the metal ions and analytes were prepared. Subsequently, 20 μL of W-CDs and 100 μL of the respective analyte solutions were added to a cuvette, and the volume was adjusted to 2 mL with distilled water. Fig. 4b highlights that PA induced the most significant

fluorescence quenching of W-CDs, whereas the PL intensity of W-CDs showed minimal changes upon the addition of other analytes. To establish further, an interference study of W-CDs for PA was conducted (Fig. S3b and c) in the presence of a different metal ions and analytes at 1 : 3 ratio which demonstrated that none of the metal ions caused significant interference with PA. Besides this, PL response of W-CDs was examined in the presence of various anions (Cl^-, I^-, AsO_4^{3-}, NO_2^-, NO_3^-, HSO_4^-, $S_2O_5^{2-}$) to assess their selectivity towards anions as shown in Fig. 4c. The findings indicated that the PL intensity of W-CDs was not influenced by the presence of these anions. The sensitivity of the nanosensor towards PA was checked by doing titrations, diluting a 1 mM stock solution to a concentration of 10^{-7} M, as shown in Fig. 4d.

3.5. Plausible mechanism of sensing

As shown in Fig. 4d, significant quenching of PL intensity of W-CDs (∼11 folds) was observed with progressive addition of PA. This observation was in coherence with the PLQY (Φ_f) values of W-CDs, which showed a sharp decrease from 29% to 2% on addition of PA to probe W-CDs, indicating the formation of a non-fluorescent [W-CDs + PA] complex as shown in Table S1. To gain a deeper understanding, several photo-
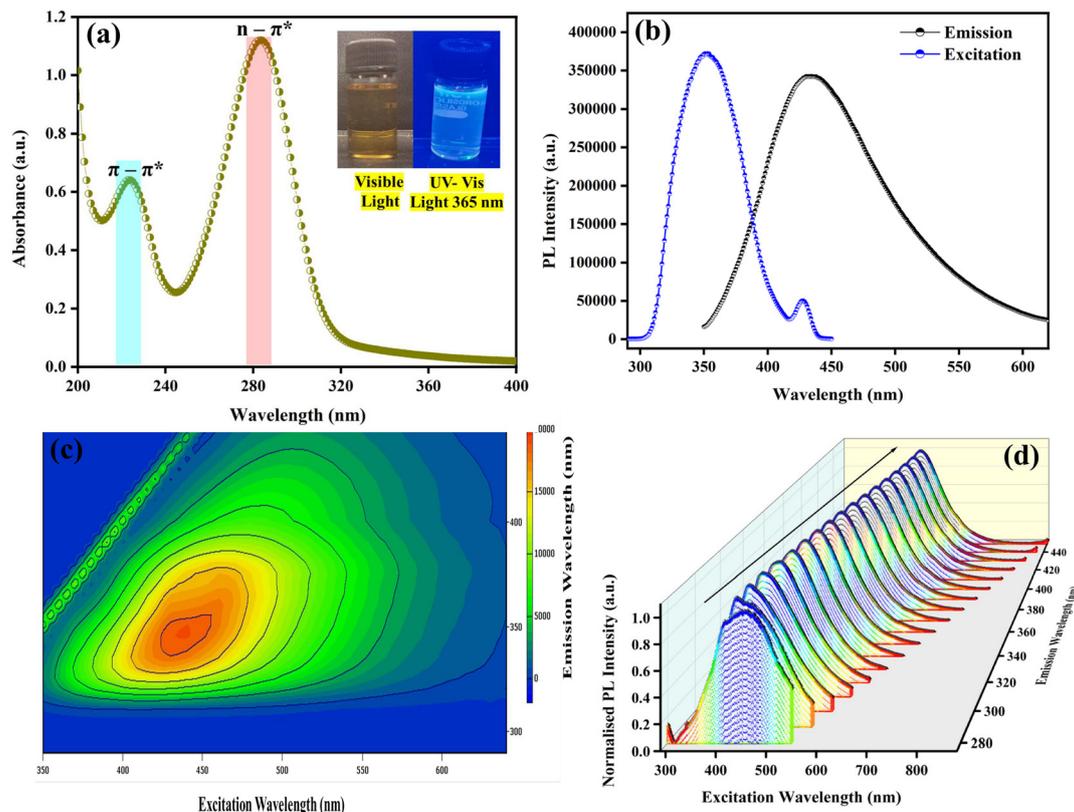
Fig. 3 (a) UV-Vis absorption spectrum of W-CDs with inset images under visible (left) and UV (right) illumination, (b) excitation and emission spectra, (c) 3D fluorescence spectra (d) normalized 3D emission spectral shift of W-CDs.

physical parameters such as the radiative rate constant (k_r), average lifetime (τ_f), and non-radiative rate constant (k_{nr}) were determined using the following equations:[62]

$$k_r = \frac{\Phi_f}{\tau_f} \tag{2}$$

$$\frac{1}{\tau_f} = k_r + k_{nr}. \tag{3}$$

The radiative rate constant (k_r) of W-CDs displayed a notable reduction, whereas the non-radiative rate constant (k_{nr}) showed a significant increase on addition of PA (Table S1), indicating the fluorescence turn-off phenomenon. The potential quenching mechanism was explored *via* a series of methodical experiments. Foremost, fluorescence lifetime measurements provided the first insight into the quenching mechanism. The average lifetime values of W-CDs (2.07 ns) and W-CDs + PA (1.94 ns) showed negligible variation (Table S1 and Fig. S4a), clearly ruling out dynamic quenching.[63,64] The minimal change instead suggests that the quenching may arise from either static interactions or the inner filter effect (IFE). To further elucidate the mechanism, the optical characteristics of W-CDs and PA were investigated thoroughly. Fig. 5a shows the excitation and emission spectra of W-CDs combined with the absorption spectrum of PA. The substantial overlap between the absorption spectrum of PA

(absorber) and the fluorescence emission spectra of W-CDs (fluorphore) satisfied the prerequisite condition for both IFE and Förster resonance energy transfer (FRET).[65] To probe further, zeta potential measurements were carried out, which revealed values of −8.45 mV for W-CDs and −9.02 mV for W-CDs + PA (Fig. S3a).[49,66] The negligible change in surface charge indicates the absence of significant electrostatic interactions, hydrogen bonding, or π–π stacking between W-CDs and PA. Since FRET requires close donor–acceptor proximity and favorable orientation, the absence of such molecular interaction effectively rules out the possibility of FRET.[62] Furthermore, the UV–Vis absorption spectra of W-CDs in the presence of PA (Fig. S4b) showed no shift, broadening, or appearance of new absorption bands. This lack of spectral change indicates that no ground-state complex or chemical interaction occurs between W-CDs and PA, thereby excluding static quenching.[64] Instead, the observed fluorescence suppression can be attributed to the inner filter effect (IFE), wherein the analyte (PA) optically attenuates the excitation or emission light of the fluorophore without altering its intrinsic properties. To quantify and validate the IFE contribution, Parker's correction analysis was employed using the Parker equation as given below:[66]

$$\frac{F_{cor}}{F_{obs}} = \frac{2.3 dA_{exc}}{1 - 10^{-dA_{exc}}} 10^{gA_{em}} \frac{2.3 sA_{em}}{1 - 10^{-sA_{em}}} \tag{4}$$
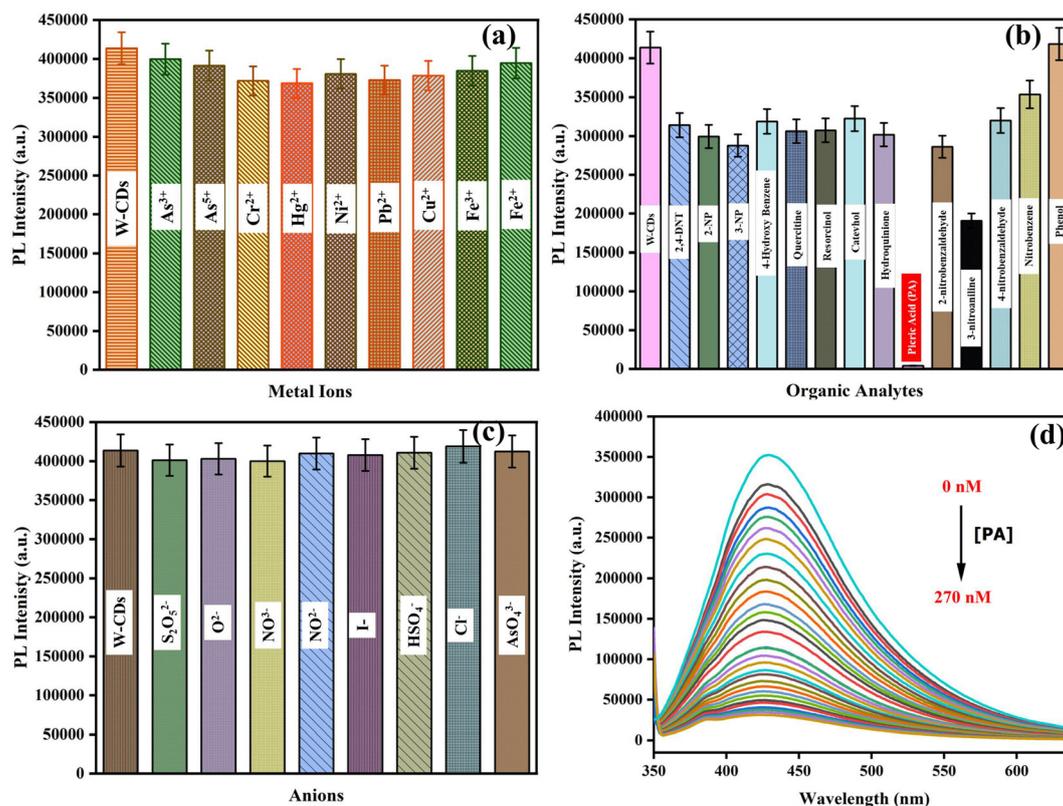
Fig. 4 Selectivity of W-CDs towards (a) metal ions, (b) organic analytes, (c) anions, and (d) fluorescence intensity variation of W-CDs at different PA concentrations.

'F_{obs}' and 'F_{cor}' represented observed photoluminiscence intensity and corrected photoluminiscence intenisty obtained by eliminating IFE from F_{obs}. 'A_{exc}' and 'A_{em}' denoted absorbance at excitation wavelength λ_{exc} 340 nm and emission wavelength, λ_{em} 432 nm respectively. s, d and g are cuvette parameters signifying thickness of the excitation beam, distance from the edge of the excitation beam to the side wall of the cuvette and breadth of the cuvette respectively, Fig. S4c. The involvement of the IFE was confirmed through the evaluation of various parameters using Parker's eqn (4), and tabulated in Table 1. The ratio of F_{cor} to F_{obs} defined as the correction factor (CF), was calculated at different concentrations of PA (Table 1). An increasing trend in CF was observed with rising concentration of PA, and the data aligned well with Parker's equation (Fig. 5b). These findings confirm that the fluorescence quenching mechanism in the W-CDs–PA sensing system is primarily governed by the IFE.[49,57] The fluorescence suppression efficiency of W-CDs in the presence of PA was evaluated using a fluorescence spectrophotometer, along with the corresponding IFE corrected values. Suppression efficiency (E) was calculated using the equation $E = 1 - F/F_0$, where F_0 and F denote the fluorescence intensities of W-CDs in the absence and presence of PA, respectively as shown in Fig. 5c.[67] The Parker's correction factor provided strong evidence that the fluorescence quenching predominantly arises from IFE rather than molecular interaction–driven mechanisms. To further

strengthen this interpretation, temperature-dependent Stern–Volmer analyses (25–55 °C) were performed (Fig. S5a). The $K_{S–V}$ values (Table S2) exhibited negligible variation across the temperature range, indicating temperature-independent behaviour of the quenching process.[68,69]

Such invariance directly supports the dominance of the inner filter effect (IFE), which stems from optical absorption phenomena rather than thermally influenced molecular interactions. Collectively, the experimental evidences firmly establishes that the fluorescence quenching of W-CDs by PA arises predominantly from the inner filter effect (Scheme 2). Additionally, quenching of the photoluminescence (PL) intensity of W-CDs was observed upon drop-casting PA onto W-CDs-coated strips when examined under UV illumination, Fig. S5b. As the volume of PA gradually increased, a corresponding decrease in PL intensity was noted. Fig. S4d depicts effect of temperature on W-CDs. Increase in temperature induces aggregation in CDs, which alters its electronic states, facilitating non-radiative decays and ultimately leading to quenching of fluorescence intensity.[70]

3.6. Determination of binding insights and LOD

To determine the stoichiometry between W-CDs and PA, Job's plot experiment was performed. The intersection point was observed at a mole fraction of 0.5, indicating a 1 : 1 stoichiometric complexation between W-CDs and PA as shown in Fig. S6a. For practical usability, an effective nanosensor must
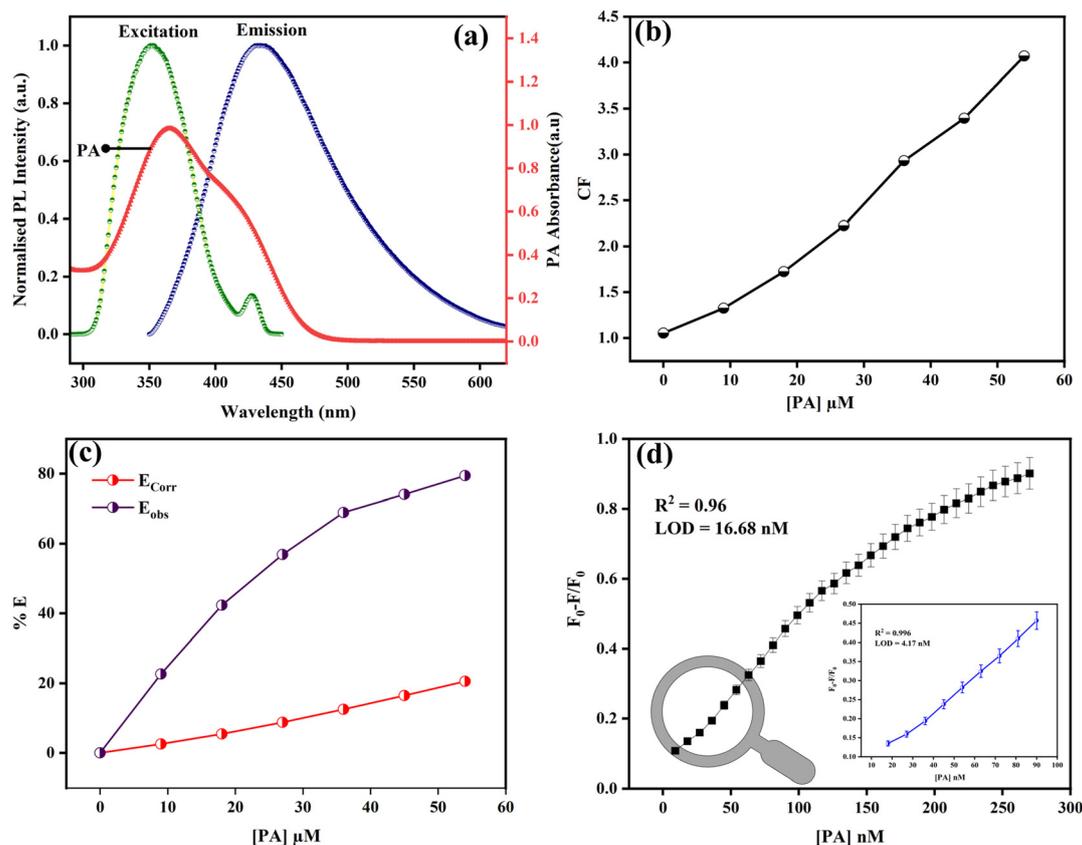
Fig. 5 (a) Overlap of PA (analyte) absorption spectrum with the excitation spectrum of W-CDs, (b) variation of CF with different concentrations of PA, (c) suppression efficiency of observed and corrected fluorescence intensities of W-CDs in the presence of PA. (d) Linear plot between PL response $(F_0 - F)/F_0$ and PA concentration (0–270 nM) with an inset showing $(F_0 - F)/F_0$ vs. PA concentration (0–100 nM).

Table 1 Deciphering various parameters governing IFE in the fluorescence quenching of W-CDs

Conc (μM)	A_{exc}	A_{em}	F_{obs}	CF	E_{obs}	E_{cor}
0	0.0396	0.0076	353 157	1.052	0	0
9	0.2452	0.0435	273 209	1.325	0.2265	0.0256
18	0.4305	0.0882	203 806	1.724	0.4231	0.0544
27	0.6475	0.1426	152 267	2.225	0.5690	0.0879
36	0.8346	0.1866	109 808	2.931	0.6891	0.1249
45	1.0554	0.2355	91 521	3.393	0.7409	0.1647
54	1.2418	0.2866	72 489	4.071	0.7948	0.2056

demonstrate both high selectivity and sensitivity to the target analyte. To assess the quenching efficiency of Picric Acid (PA), Stern–Volmer constant (K_{S-V}) was deduced using 1 : 1 stoichiometry the equation given below:[71]

$$\frac{F_0}{F} = 1 + K_{S-V}[Q]. \tag{5}$$

The slope of plot between $\frac{F_0}{F}$ against concentration of quencher [PA] gave the quenching constant (K_{S-V}), whereas F and F_0 represents PL intensity of W-CDs, with and without quencher and [Q] denotes the quencher concentration, PA. The quenching constant K_{S-V} was determined to be 0.0074 nM^{-1}

(eqn (5), Fig. S6b) with a correlation coefficient, R^2 of 0.98, indicating that the nanosensor exhibits a satisfactory linearity range. Furthermore, to deduce the limit of detection, a linear plot between, $F_0 - F/F_0$ and concentration of PA was plotted (Fig. 5d) over a range of (0–270 nM) and limit of detection was estimated using $3\sigma/K$ where K and σ, refers to slope and standard deviation of intercept respectively. The experiment was repeated thrice. Error bars represent the standard error of measurements obtained from three independent experiments. The inset image of Fig. 7b showed LOD of 4.17 nM for linearity range 10–90 nM with R^2 of 0.99. The fabricated nanosensor demonstrates significantly lower detection limits (Table 2) as other reported sensors in the literature. To determine the stoichiometric ratio of W-CDs to PA and assess the interaction and binding affinity between W-CDs and PA in the excited state, the binding constant was estimated by analyzing the corresponding fluorescence intensity and applying the 1 : 1 linear Benesi–Hildebrand equation:[71]

$$\frac{1}{F_0 - F} = \frac{1}{F_0 - F_1} + \frac{1}{K[Q](F_0 - F_1)} \tag{6}$$

where 'F_0' and 'F' denotes PL intensity of W-CDs in absence and presence of PA, 'Q' and 'F_1' represents quencher (PA) concentration and intensity of W-CDs@PA complex. The binding constant 'K' (eqn (6), Fig. S6c) was deduced by taking the reci-
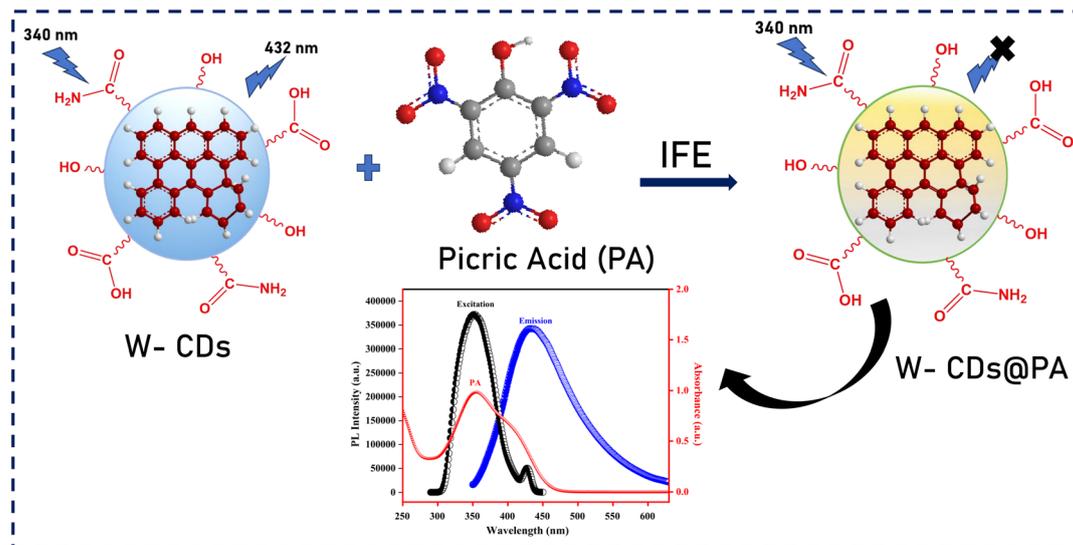
Scheme 2 Proposed mechanism of PA detection *via* inner filter effect.

Table 2 Comparison of biomass derived CDs based sensing systems for PA detection

Sr. no.	Precursor	Linear range	Synthesis method	Time (h)	QY (%)	LOD	Ref.
1	Coffee residue	0–0.02 μM	Pyrolysis & etching	2	—	0.26 μM	31
2	Soy sauce	0.2–24 μM	Column chromatography	—	5.7	70 nM	32
4	Betel leaf	0.3–3.3 μM	Hydrothermal	12	4.21	0.135 μM	33
3	Grape skin	0.06–79.4 μM	Hydrothermal	3	18.6	10 nM	34
5	Discarded glycerol	0–7.2 μM	Hydrothermal	5		1.07 μM	35
6	Mushroom	1–10 μM	Hydrothermal	8	2	13.5 nM	36
7	Okra leaves	4–30 μg mL^{-1}	Pyrolysis & reflux	3.5	12	2.2 μg mL^{-1}	37
8	Watermelon extract	10–90 nM	Hydrothermal	3	29	4.17 nM	Present work

procal of slope value of $\frac{1}{F_0 - F}$ *versus* $\frac{1}{Q}$ plot which came out to be 2232 nM^{-1}.

3.7. Precision and accuracy examination

Interday and intraday precision of probe, W-CDs was evaluated by determining the error and relative standard deviation (% RSD). This study was performed in triplicates at different concentrations. An error below 1% confirmed the precision of the designed sensor (Table S3). Assessing the precision and accuracy of a nanosensor through intraday and interday measurements over a three-day period is essential for ensuring its consistent and reliable performance. Intraday evaluations measure short-term consistency, whereas interday assessments evaluate temporal stability. This procedure verifies that the sensor yields precise and consistent findings, which is crucial for its practical deployment in real-world applications.

3.8. Performance assessment on real samples

The efficacy and performance of the designed nanosensor model was validated as per ICHQ2(R1) guidelines. Tap water (source: chemistry laboratory) and river water (source: Bhakhra River, Patiala, Punjab, India) samples were tested by spiking them with a known concentration of the analyte (PA). The

Table 3 Practical application of the developed W-CDs probe for PA detection in real samples

Sample	Spiked conc. (nM)	Conc. found (nM)	% recovery	% RSD
Tap water	33	35.64	108	0.37
	66	67.3	101	1.39
	99	96.9	97.8	0.97
	132	126.5	95.8	1.51
River water	33	37	112	0.79
	66	70.4	106.6	0.38
	99	105.8	106.8	0.03
	132	138.9	105.2	1.27

recovery percentage and relative SD values were calculated and acceptable results were obtained (Table 3).

4. Integration of smart sensor into a portable detection device

Furthermore, attempts have been made to create a portable, reasonably priced electronic device incorporating spectro-

scopic sensors to measure the amounts of picric acid in test materials. The device's effectiveness as a dependable detector for picric acid in these samples strongly correlates with experimental results. This study lays the foundation and groundwork for developing a portable device by utilizing watermelon extract-derived W-CDs for picric acid.

4.1. Design insights into the portable sensor device

This part of the paper concentrates on the tailored design of an optical signal-driven sensor for detecting nitroaromatic compounds, specifically PA, employing light sources and detectors functioning within the ultraviolet (UV), visible (VIS), and near-infrared (NIR) spectral ranges. The study examined the optimal light wavelengths for precisely measuring the concentration of PA in a stock solution of W-CDs. In this study, the signal from UV excitation source passed through the W-CDs sample and measured by the detectors in terms of interactance. Interactance is a technique of spectral analysis in which the light interacts with a sample, and the emitted light is measured at a particular distance from the source, on the same side of the sample. The UV light sources showed a lower absorption in samples containing PA as compared to mid-infrared (MIR) and VIS-NIR light. Therefore, UV sensor performed better to detect the reflected light through the sample over mid-infrared (MIR) and VIS-NIR sensors.

The robust spectrophotometer SparkFun Triad Spectroscopy Sensor, shown in Fig. S7, features three AS7265x spectral sensors and LEDs spanning the visible, ultraviolet (UV), and infrared (IR) light ranges. It has three miniature sensors (AS72651, AS72652, and AS72653) internally with each of them having an iris, optical filters and a photodiode array which enables the capturing of a wide spectrum of 410 nm (UV) to 940 nm (IR). Although the wavelength of UV source ranges from 100 nm to 400 nm, the suggested sensor addresses the top limits of the wavelength of UV source. The system measures 18 wavebands with a 20 nm full width at half maximum (FWHM) and reaches a precision of 28.6 nW cm^{-2}

with a ±12% margin of error.[72] The spectroscopy sensor fosters the ability to explore the interaction between test material and light. The microcontroller ESP32 interfaced with AS7265x spectral sensor controls the measurement process through Arduino-IDE programming. The AS7265x communicates with the microcontroller using I2C protocol's external modules. In this protocol, the sensor's power and ground pins are connected to the ESP32's 3.3 V and ground pins, respectively. Likewise, the SCL and SDA pins of the sensor are connected to GPIO 22 and GPIO 21 pins of the ESP32, respectively. It operates on 3.3 V, which is ideal for the I2C port. The interfacing between ESP32 microcontroller and AS7265x spectral sensor is illustrated in Fig. S7. The electronic circuit including the spectroscopy sensor of portable device requires only +3.3 V to +5 V DC for its functioning. It is powered through USB port connected to computing machine (laptop) during the measurement process only. Due to a low power device, it can work continuously for several hours for testing.

Fig. 6a shows a schematic flow representation of the methodology. The sensor and cuvette are housed in a 3D-printed case and protected with black electrical tape to avoid any unwanted disturbance through external light source during measurement (Fig. 6b and c). The experimental setup for testing a portable device to detect nitroaromatics in W-CDs is shown in Fig. 6d. During testing, UV light shines on the W-CDs sample with different amounts of picric acid. The sensor detects how much light is reflected after the sample absorbs it. As picric acid levels go up, the sensor readings drop. This happens due to the quenching of PL intensity of W-CDs, where light intensity decreases with more picric acid.

4.2. 3D model of the device structure

Before conducting any experimental activity, an enclosure is required to fix the housing of the AS7265x sensor module, cuvette and interconnection of microcontroller. A 3D-printable structure is designed using Tinkercad software. The external dimensions of this structure have been determined by aligning
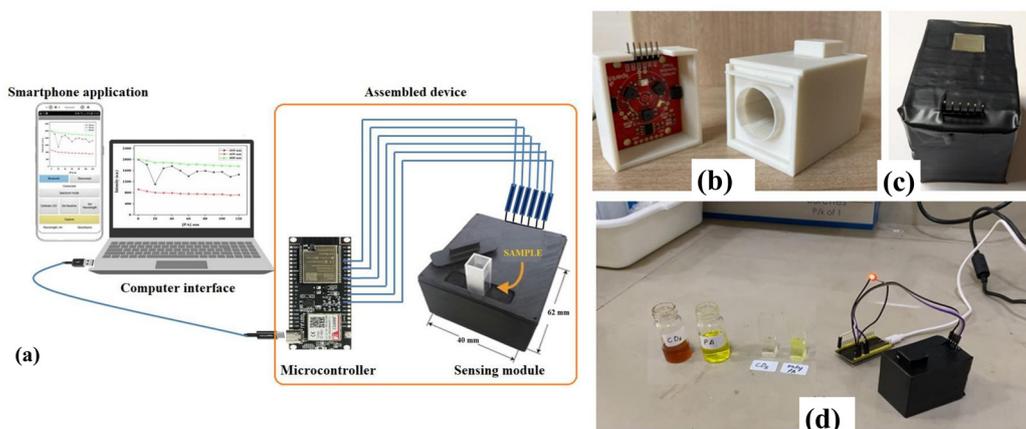

Fig. 6 (a) Schematic representation of the methodology flow (b) sensor placement in portable device, (c) enclosure with sensor protected with black electrical tape and (d) experimental setup.

with the sensor's width, length, and height, measuring 45 mm × 45 mm × 72.5 mm. The designated dimensions for the cuvette placement are 17.5 mm × 17.5 mm × 8.25 mm. Fig. S10 illustrates the design process steps for creating a 3D structure model prior to the actual printing stage using Tinkercad software tool. The enclosure is then printed using 3D printer machine and components are assembled to make it a complete device for measuring of picric acid in a test sample.

4.3. Methodology

The details of the experimental apparatus are provided in the SI.

4.4. Optimal wavelength selection for picric acid

The Triad Sensor collected light data at 18 wavelengths to help detect picric acid. The AS7265x sensor turned this light data into digital signals. Arduino IDE (microcontroller) read and stored the data from each trial for later use. The W-CDs mixed with PA absorb more UV light, so UV light sources work best. The detector first measured light at 410 nm, 435 nm, and 460 nm using distilled water under UV light. Light intensity depends on two things scattering and absorption by the sample and both these factors are wavelength dependent. The higher PA levels lead to more absorption at all three wavelengths, lowering detected light as shown in Fig. S8a, tabulated in Table S3. The Fig. S8a shows how light intensity drops across these wavelengths. As shown in Fig. S8b, the emission intensity at 435 nm emerges as the most suitable choice for the experiment, displaying better linearity across different PA concentrations compared to the signals at 410 nm and 460 nm. In this experiment, initially the device is exposed to the W-CDs solution only, which resulted in a high digital output for 435 nm as recorded in Table S3. From each step now onward, the concentration of picric acid is increased by 10 nM, and the output of device shows quenching and smaller output values are recorded in every step linearly. The concentration of picric acid is varied from 0 nM to 120 nM in 12 equal steps. After 120 nM concentration of picric acid, the output of device becomes unstable. This experiment is conducted thrice to validate the stability performance of the sensor. Therefore, the proposed device is suitable for stable and linear detection of the picric acid concentration range from 0 nM to 120 nM. The portable sensor gave results similar to those from a standard photoluminescence spectrophotometer Fig. S8c. These experimental findings, along with validation steps, highlight the effectiveness of the spectroscopy-based portable sensor in reliably detecting PA in the test samples. Besides this, a qualitative demonstration of PA detection in test samples was carried out using the portable device, as shown in the video, Scheme S1.

4.5. Sample preparation

In this work, carbon dots were synthesised from watermelon extract using an environmentally benign microwave-assisted technique, abbreviated as W-CDs. A 1 mM stock solution of different nitroaromatic analytes was made in deionized water in order to assess the selectivity of W-CDs. A cuvette was used to analyse the emission spectra after 20 μL of W-CDs was introduced to 2000 μL of deionized water and 1 mM of the analyte solution for the purpose of selectivity testing. The stock solution used for the sensitivity study included 0.1 μM of picric acid.

4.6. Interference study of portable device

Interference studies were carried out to validate the selectivity of the W-CDs-based probe toward PA in the presence of potential interfering analytes. In this experiment, PA and each additional analyte (2-nitrophenol and 2,4-dinitrotoluene) were introduced in a 1 : 3 ratio (100 μL of PA and 300 μL of interferent). The PL intensity was recorded using the developed portable sensor at three wavelength filters. From Table S4, it is observed that for the test sample of W-CDs (Blank), the device record a high value at the output. But as soon as, the PA (100 μL) is added in to test sample, the output value of device shows quenching and records a significant smaller value. Notably, a significant quenching in PL intensity was observed exclusively in the presence of PA, indicating the probe's strong selectivity for it. The presence of other analytes did not cause any considerable interference in the detection of PA, as demonstrated in Fig. S9. These results show consistency with observations obtained through conventional spectrofluorometric analysis (Fig. S3b and S3c).

4.7. Comparison of portable device with standard spectrofluorometer

To validate the selectivity, sensitivity and stability performance of the portable sensor, multiple experiments were conducted. Foremost, the device is tested to identify a specific wavelength which can accurately detect the presence of picric acid in W-CDs (Fig. S8a and Table S3). The result of this experiment demonstrated that the developed device shows a linear performance with good sensitivity for detection of picric acid at the wavelength of 435 nm (Fig. S8b). The experiment has been repeated thrice and similar results were recorded. This validates the stability of the portable device. The performance of the portable device at 435 nm is quite comparable to the performance of standard spectrofluorometer in UV range as shown in Fig. S8c. The selectivity performance of the portable device is validated through interference study. In this activity, the efficiency of portable device is measured to detect picric acid in the presence of potential interfering analytes such as 2-nitrophenol and 2,4-dinitrotoluene (Fig. S9a, b and Table S5). The experiment results verifies that portable sensor can detect the presence of picric acid exclusively even in presence of any interfering analyte. Limit of detection of portable device was calculated using $3\sigma/K$ and was found out to be 24 nM (Fig. S9c). All these experimental studies firmly establish the proficiency of portable sensor in detection and quantifying picric acid in W-CDS.

5. Design of logic gate

For molecular computation, designing logic gates with electronic circuits at the nanoscale is essential. By using physico-
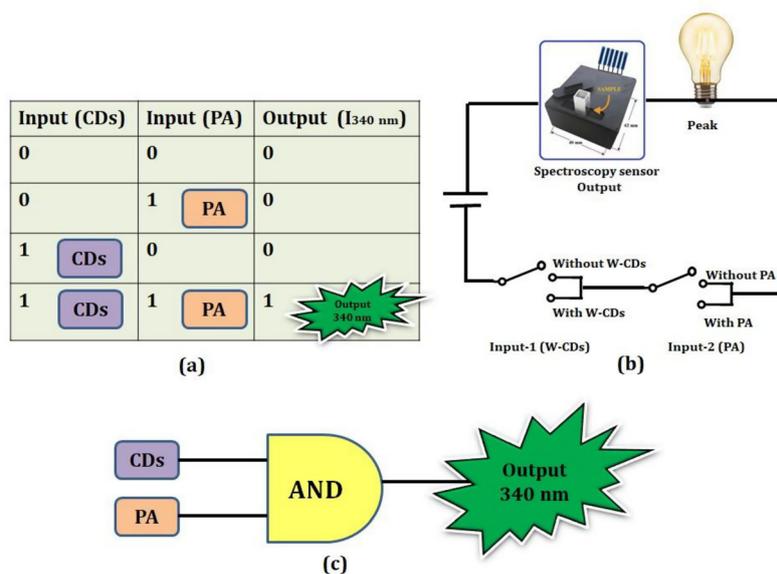
Fig. 7 Designing of AND logic gate based on the optical response received at 340 nm using developed spectroscopy sensor device with two inputs CDs and PA (a) truth table, (b) logic implementation, and (c) schematic representation.

chemical and biological changes as inputs to perform Boolean arithmetic operations, molecular logic gates mimic electronic circuits. These logic gates are built using a probe's fluorescence response to different analytes, which results in matching variations in fluorescence intensity. We have created basic logic operations, like the AND gate, by examining the spectral variances of W-CDs and PA through the developed spectroscopy sensor device.

5.1. Two-input logic gate implementation

AND gate. This two-input logic gate only produces a true output when both of its inputs are true. Optical sensors based on CDs have been extensively investigated for a number of uses, such as circuits, memory devices, keypad locks, and logic gates with one or more inputs. An AND gate is created when a quencher and a fluorescence recovery agent are used as inputs in a two-input logic gate. Feng *et al.* created spermin-functionalized carbon dots (SC-dots) with numerous logic systems, demonstrating one of the first uses of CDs in molecular logic gates.[73] In the presence of D-penicillamine, Yuan *et al.* used fluorescence recovery in the c-dots/Hg^{2+} system to create an AND logic gate.[74] A red-emissive CDs with dual readout capabilities for AND logic operations was presented by Gao *et al.*[75] Gao *et al.* also described another AND gate with glutathione and Cu^{2+} as inputs, in which the addition of glutathione restored the fluorescence quenching caused by Cu^{2+}.[76] More recently, Liu *et al.* used a multimode sensor for Cu^{2+} and L-cysteine to create an AND molecular logic gate.[77]

The electronic logic based on W-CDs and its sensing response is covered in this part. The proposed AND gate works on the basis of fluorescence recovery, which states that when PA is added, the quenched fluorescence of W-CDs is recovered, Fig. 7b. The authors describe a multimode sensing method

that includes colour changes, absorption intensity shifts, peak shifts, and fluorescence intensity changes. Four different output modes were examined using two inputs such as W-CDs and PA as shown in Fig. 7a. A matching truth table was created (Fig. 7a). Notably, a dual-input approach is used when creating an AND gate, with CDs acting as one input and an analyte (PA), which quenches fluorescence, acting as the second input. The logic AND gate implementation by developed spectroscopy sensor is illustrated in Fig. 7c. The result shows that the developed spectroscopy sensor is able to validate the logic gate response successfully.

6. Conclusion

In summary, this study introduces a sustainable and cost-effective approach for synthesizing highly water-soluble, biomass-derived carbon dots from watermelon extract (W-CDs) *via* hydrothermal green route, without the need for chemical additives. The synthesized W-CDs exhibited excellent optical properties, including a notable fluorescence quantum yield of 29% and vivid cyan emission under UV light. These features enabled their application as an ultra-sensitive and selective "turn-off" fluorescent probe for detecting picric acid (PA), achieving a low detection limit of 4.17 nM in aqueous media. Mechanistic analysis confirmed that the sensing mechanism is predominantly driven by the inner filter effect (IFE), supported by spectral overlap and consistent fluorescence lifetimes in the presence of PA. To demonstrate practical applicability, a portable, microcontroller-based fluorometric device incorporating W-CDs was developed. The device's performance closely matched conventional spectroscopic methods, validating its analytical precision. Moreover, interference studies

affirmed the high selectivity of W-CDs for PA, even amidst structurally related compounds. The incorporation of a fluorescence-based AND logic gate further highlights the system's potential in smart sensing applications. Overall, this study presents a robust, eco-friendly, and portable sensing platform for the sensitive detection of nitroaromatic explosives, with strong potential for real-world applications in environmental monitoring and public safety.

Author contributions

Mallika Phull, Amjad Ali and Banibrata Maity were responsible for the synthesis, characterization, and sensing studies of the W-CDs. Jobanpreet Brar and Amit Mishra designed and implemented the electronics and microcontroller-based fluorometric device and logic gate. All authors contributed to data interpretation and manuscript preparation.

Conflicts of interest

The authors declare that they don't have any conflict of interest in the publication of the manuscript.

Data availability

All data supporting the findings of this study are available within the article and its supplementary information (SI). Supplementary information: Fig. S1 shows volume optimisation, slit width optimisation and HRTEM images of W-CDs at 50 nm resolution. Fig. S2 presents excitation wavelength dependent emission spectra, emission spectra of W-CDs at varying pH (2–12), photostability assessment of W-CDs over irradiation time and effect of ionic strength on PL Intensity of W-CDs at different NaCl concentrations. Fig. S3 depicts zeta analysis of W-CDs and W-CDs in presence of PA, interference study of W-CDs for PA in presence of different metal ions and organic analytes. Fig. S4 displays Fluorescence lifetime decay of W-CDs in the presence of PA, UV-Vis absorption spectra of W-CDs in presence of PA, schematic geometry of IFE fluorescence correction measurements and effect of temperature on W-CDs. Fig. S5 shows temperature dependent K_{S-V} determination and visual depiction of PL quenching of PA on W-CDs coated strips. Fig. S6 depicts Job's Plot, Stern–Volmer plot of W-CDs, B–H plot illustrating the interaction between PA and W-CDs. Fig. S7 demonstrates Interfacing circuit between microcontroller ESP32 and spectral sensor. Fig. S8 displays normalised intensity at UV detector for three wavelengths (410 nm, 435 nm, and 460 nm) reflected from sample at different PA concentrations, intensity of different PA concentrations for wavelength 435 nm at UV detector and instrument result verification by portable device data. Fig. S9 shows interference study of W-CDs for PA in presence of different metal ions by portable device and LOD evaluation by portable device. Fig S10 shows 3D print design of deivce housing using

Tinkercad. Table S1 shows photophysical parameters of W-CDs in presence of PA. Table S2 shows temperature-dependent variation of quenching constant (K_{S-V}) for the W-CDs–PA system. Table S3 displays intraday and interday precision data for PA estimation using the developed W-CDs sensor. Table S4 tabulates UV detector data at three wavelengths (410 nm, 435 nm, and 460 nm) for PA in portable device. Table S5 demonstrates Interference study by portable device; Scheme 1 shows video depicting qualitative detection of PA in test sample by portable device; Section 4.3. The details of methodology for portable device testing. See DOI: https://doi.org/10.1039/d5nr03407h.

Acknowledgements

References

1 K. S. Ju and R. E. Parales, *Microbiol. Mol. Biol. Rev.*, 2010, **74**, 250–272, DOI: 10.1128/mmbr.00006-10.

2 M. Rong, L. Lin, X. Song, T. Zhao, Y. Zhong, J. Yan and X. Chen, *Anal. Chem.*, 2015, **87**, 1288–1296, DOI: 10.1021/ac5039913.

3 Y. Salinas, R. Martínez-Máñez, M. D. Marcos, F. Sancenón, A. M. Costero, M. Parra and S. Gil, *Chem. Soc. Rev.*, 2012, **41**, 1261–1296, DOI: 10.1039/C1CS15173H.

4 M. E. Germain and M. J. Knapp, *Chem. Soc. Rev.*, 2009, **38**, 2543–2555, DOI: 10.1039/B809631G.

5 L. Lin, M. Rong, S. Lu, X. Song, Y. Zhong, J. Yan and X. Chen, *Nanoscale*, 2015, **7**, 1872–1878, DOI: 10.1039/C4NR06365A.

6 D. M. Badgujar, M. B. Talawar, S. N. Asthana and P. P. Mahulikar, *J. Hazard. Mater.*, 2008, **151**, 289–305, DOI: 10.1016/j.jhazmat.2007.10.039.

7 M. Liu and W. Chen, *Biosens. Bioelectron.*, 2013, **46**, 68–73, DOI: 10.1016/j.bios.2013.01.073.

8 M. E. Walsh, *Talanta*, 2001, **54**, 427–438, DOI: 10.1016/S0039-9140(00)00541-5.

9 K. Bratin, P. T. Kissinger, R. C. Briner and C. S. Bruntlett, *Anal. Chim. Acta*, 1981, **130**, 295–311, DOI: 10.1016/S0003-2670(01)93007-7.

10 H. X. Zhang, A. M. Cao, J. S. Hu, L. J. Wan and S. T. Lee, *Anal. Chem.*, 2006, **78**, 1967–1971, DOI: 10.1021/ac051826s.

11 L. Agüí, D. Vega-Montenegro, P. Yáñez-Sedeño and J. M. Pingarrón, *Anal. Bioanal. Chem.*, 2005, **382**, 381–387, DOI: 10.1007/s00216-004-3017-z.

12 C. Mullen, A. Irwin, B. V. Pond, D. L. Huestis, M. J. Coggiola and H. Oser, *Anal. Chem.*, 2006, **78**, 3807–3814, DOI: 10.1021/ac060190h.

13 H. Sohn, M. J. Sailor, D. Magde and W. C. Trogler, *J. Am. Chem. Soc.*, 2003, **125**, 3821–3830, DOI: 10.1021/ja021214e.

14 G. Wang, M. Li, Q. Wei, Y. Xiong, J. Li, Z. Li and H. Tu, *ACS Sens.*, 2021, **6**, 1849–1856, DOI: 10.1021/acssensors.1c00047.

15 W. Jiang, L. Xia, D. Li, P. Wu, T. Zou, X. Yuan and J. Wang, *Biosensors*, 2022, **12**, 682, DOI: 10.3390/bios12090682.

16 Y. Fan, Y. Chen, Y. Bai, B. An and J. Xu, *Nanomaterials*, 2022, **12**, 4034, DOI: 10.3390/nano12224034.

17 L. M. Shen and J. Liu, *Talanta*, 2016, **156**, 245–256, DOI: 10.1016/j.talanta.2016.05.028.

18 M. J. Molaei, *Talanta*, 2019, **196**, 456–478, DOI: 10.1016/j.talanta.2018.12.042.

19 D. G. Babar and S. S. Garje, *ACS Omega*, 2020, **5**, 2710–2717, DOI: 10.1021/acsomega.9b03234.

20 C. Ji, Y. Zhou, R. M. Leblanc and Z. Peng, *ACS Sens.*, 2020, **5**, 2724–2741, DOI: 10.1021/acssensors.0c01556.

21 J. F. Y. Fong, S. F. Chin and S. M. Ng, *Biosens. Bioelectron.*, 2016, **85**, 844–852, DOI: 10.1016/j.bios.2016.05.087.

22 S. Pandit, T. Banerjee, I. Srivastava, S. Nie and D. Pan, *ACS Sens.*, 2019, **4**, 2730–2737, DOI: 10.1021/acssensors.9b01227.

23 F. Gao, S. Ma, J. Li, K. Dai, X. Xiao, D. Zhao and W. Gong, *Carbon*, 2017, **112**, 131–141, DOI: 10.1016/j.carbon.2016.10.089.

24 Y.-P. Sun, B. Zhou, Y. Lin, W. Wang, K. A. S. Fernando, P. Pathak, M. J. Meziani, B. A. Harruff, X. Wang, H. Wang, P. G. Luo, H. Yang, M. E. Kose, B. Chen, L. M. Veca and S.-Y. Xie, *J. Am. Chem. Soc.*, 2006, **128**, 7756–7757, DOI: 10.1021/ja062677d.

25 S. Chernyak, A. Podgornova, S. Dorofeev, S. Maksimov, K. Maslakov, S. Savilov and V. Lunin, *Appl. Surf. Sci.*, 2020, **507**, 145027, DOI: 10.1016/j.apsusc.2019.145027.

26 K. Hagiwara, S. Horikoshi and N. Serpone, *Chem. – Eur. J.*, 2021, **27**, 9466–9481, DOI: 10.1002/chem.202100823.

27 Z. M. Khan, R. S. Rahman, S. Islam and M. Zulfequar, *Opt. Mater.*, 2019, **91**, 386–395, DOI: 10.1016/j.optmat.2019.03.054.

28 A. M. Alex, M. D. Kiran, G. Hari, A. Krishnan, J. S. Jayan and A. Saritha, *Mater. Today: Proc.*, 2019, **26**, 716–719, DOI: 10.1016/j.matpr.2019.12.409.

29 M. Phull, A. Ali and B. Maity, *RSC Sustainability*, 2024, **2**, 1599–1612, DOI: 10.1039/D4SU00004H.

30 S. Yıkmış, *J. Food Meas. Charact.*, 2020, **14**, 1417–1426, DOI: 10.1007/s11694-020-00391-7.

31 S. Zong, B. Wang, W. Ma, Y. Yan and J. Li, *Chem. Res. Chin. Univ.*, 2021, **37**, 623–628, DOI: 10.1007/s40242-021-1028-3.

32 L. Yang, J. Ma and B. Yang, *J. Fluoresc.*, 2023, **33**, 1981–1993, DOI: 10.1007/s10895-023-03207-1.

33 K. Kalanidhi and P. Nagaraaj, *J. Photochem. Photobiol., A*, 2021, **418**, 113369, DOI: 10.1016/j.jphotochem.2021.113369.

34 J. Li, L. Zhang, P. Li, Y. Zhang and C. Dong, *Sens. Actuators, B*, 2018, **258**, 580–588, DOI: 10.1016/j.snb.2017.11.096.

35 D. Poddar, B. Mahilary, K. Patir and S. Basumatary, *NanoTrends*, 2025, **11**, 100146, DOI: 10.1016/j.nwnano.2025.100146.

36 D. J. Britto, Y. Vadivelu, M. Rajkumar, M. A. Jhonsi and A. Kathiravan, *Inorg. Chem. Commun.*, 2025, **183**, 115789, DOI: 10.1016/j.inoche.2025.115789.

37 S. V. Koparde, O. S. Nille, A. G. Kolekar, P. P. Bote, K. V. Gaikwad, P. V. Anbhule and G. B. Kolekar, *Spectrochim. Acta, Part A*, 2024, **321**, 124659, DOI: 10.1016/j.saa.2024.124659.

38 A. Thakur and P. Devi, *Crit. Rev. Anal. Chem.*, 2024, **54**, 193–218, DOI: 10.1080/10408347.2022.2070838.

39 A. F. Silva, K. Löfkvist, M. Gilbertsson, E. van Os, G. Franken, J. Balendonck and R. C. Martins, *Chem. Proc.*, 2021, **5**, 88, DOI: 10.3390/CSAC2021-10448.

40 L. G. Pap, *J. Chem. Educ.*, 2021, **98**, 2584–2591, DOI: 10.1021/acs.jchemed.0c01345.

41 L. M. Díaz-Vázquez, B. M. Ortiz-Andrade, M. L. Kovarik and M. L. Morris, in *Active Learning in the Analytical Chemistry Curriculum*, American Chemical Society, Washington, DC, 2022, 181–204. DOI: 10.1021/bk-2022-1409.ch011.

42 N. Emmanuel, R. B. Nair, B. Abraham and K. Yoosaf, *J. Chem. Educ.*, 2021, **98**, 1590–1595, DOI: 10.1021/acs.jchemed.0c01028.

43 H. Han, D. H. Jung, H. J. Kim, T. S. Lee, H. S. Kim, H. Y. Kim and S. H. Park, *J. Sens.*, 2020, **1**, 9251416, DOI: 10.1155/2020/9251416.

44 R. El-Shaheny, L. A. Al-Khateeb, M. A. El Hamd and M. El-Maghrabey, *Anal. Chim. Acta*, 2021, **1172**, 338684, DOI: 10.1016/j.aca.2021.338684.

45 R. El-Shaheny, L. A. Al-Khateeb and M. El-Maghrabey, *Sens. Actuators, B*, 2021, **348**, 130657, DOI: 10.1016/j.snb.2021.130657.

46 L. A. Al-Khateeb, M. El-Maghrabey and R. El-Shaheny, *Spectrochim. Acta, Part A*, 2023, **302**, 123109, DOI: 10.1016/j.saa.2023.123109.

47 O. Akhavan, *Carbon*, 2015, **81**, 158–166, DOI: 10.1016/j.carbon.2014.09.044.

48 S. Thambiraj and R. Shankaran, *Appl. Surf. Sci.*, 2016, **390**, 435–443, DOI: 10.1016/j.apsusc.2016.08.106.

49 N. Sohal, S. Sharma, D. Choudhury, S. Basu and B. Maity, *ACS Appl. Bio Mater.*, 2023, **6**, 4846–4855, DOI: 10.1021/acsabm.3c00594.

50 K. Kasinathan, S. Samayanan, K. Marimuthu and J. H. Yim, *Appl. Surf. Sci.*, 2022, **601**, 154266, DOI: 10.1016/j.apsusc.2022.154266.

51 B. K. John, N. John, B. K. Korah, C. Thara, T. Abraham and B. Mathew, *J. Photochem. Photobiol., A*, 2022, **432**, 114060, DOI: 10.1016/j.jphotochem.2022.114060.

52 X. Chen, X. Wang and D. Fang, *Fullerenes, Nanotubes Carbon Nanostruct.*, 2020, **28**, 1048–1058, DOI: 10.1080/1536383X.2020.1794851.

53 X. Hu, Y. Li, Y. Xu, Z. Gan, X. Zou, J. Shi, X. Huang, Z. Li and Y. Li, *Food Chem.*, 2021, **339**, 127775, DOI: 10.1016/j.foodchem.2020.127775.

54 X. Hou, J. Song, Q. Wu and H. Lv, *Anal. Chim. Acta*, 2021, **1184**, 339012, DOI: 10.1016/j.aca.2021.339012.

55 N. Thongsai, N. Tanawannapong, J. Praneerad, S. Kladsomboon, P. Jaiyong and P. Paoprasert, *Colloids Surf., A*, 2019, **560**, 278–287, DOI: 10.1016/j.colsurfa.2018.09.077.

56 H. Ding, S. B. Yu, J. S. Wei and H. M. Xiong, *ACS Nano*, 2016, **10**, 484–491, DOI: 10.1021/acsnano.5b05406.

57 H. R. Nan, Y. H. Liu, W. J. Gong, H. B. Peng, Y. Q. Wang, Z. B. Zhang and X. H. Cao, *Anal. Methods*, 2022, **14**, 532–540, DOI: 10.1039/D1AY02017J.

58 Z. Gan, H. Xu and Y. Hao, *Nanoscale*, 2016, **8**, 7794–7807, DOI: 10.1039/C6NR00605A.

59 R. Bandi, B. R. Gangapuram, R. Dadigala, R. Eslavath, S. S. Singh and V. Guttena, *RSC Adv.*, 2016, **6**, 28633–28639, DOI: 10.1039/C6RA01669C.

60 P. S. R. Prasad, K. S. Prasad and N. K. Thakur, *Curr. Sci.*, 2006, **91**, 1544–1547.

61 A. Kumari, A. Kumar, S. K. Sahu and S. Kumar, *Sens. Actuators, B*, 2018, **254**, 197–205, DOI: 10.1016/j.snb.2017.07.157.

62 J. R. Lakowicz, *Principles of Fluorescence Spectroscopy*, Springer, Boston, 3rd edn, 2006. DOI: 10.1007/978-0-387-46312-4.

63 F. Cheng, X. An, C. Zheng and S. Cao, *RSC Adv.*, 2015, **5**, 93360–93363, DOI: 10.1039/C5RA17742K.

64 Y. Z. Fan, Y. Zhang, N. Li, S. G. Liu, T. Liu, N. B. Li and H. Q. Luo, *Sens. Actuators, B*, 2017, **240**, 949–955, DOI: 10.1016/j.snb.2016.09.143.

65 W. Dong, R. Wang, X. Gong and C. Dong, *Anal. Bioanal. Chem.*, 2019, **411**, 6687–6695, DOI: 10.1007/s00216-019-02019-2.

66 F. Zu, F. Yan, Z. Bai, J. Xu, Y. Wang, Y. Huang and X. Zhou, *Microchim. Acta*, 2017, **184**, 1899–1914, DOI: 10.1007/s00604-017-2235-2.

67 F. Yan, F. Zu, J. Xu, X. Zhou, Z. Bai, C. Ma and L. Chen, *Sens. Actuators, B*, 2019, **287**, 231–240, DOI: 10.1016/j.snb.2019.02.056.

68 J. Tang, Y. Zhang, Y. Liu, D. Liu, H. Qin and N. Lian, *RSC Adv.*, 2019, **9**, 38174–38182, DOI: 10.1039/C9RA08477K.

69 P. B. K. Chau, T. H. Vu and M. I. Kim, *Nanomaterials*, 2023, **13**, 2444, DOI: 10.3390/nano13172444.

70 Y. Ru, G. I. Waterhouse and S. Lu, *Aggregate*, 2022, **3**(6), e296, DOI: 10.1002/agt2.296.

71 H. A. Benesi and J. H. Hildebrand, *J. Am. Chem. Soc.*, 1949, **71**, 2703–2707, DOI: 10.1021/ja01176a030.

72 N. T. Tran and M. Fukuzawa, *Sensors*, 2020, **20**(20), 5883, DOI: 10.3390/s20205883.

73 L. Feng, A. Zhao, J. Ren and X. Qu, *Nucleic Acids Res.*, 2013, **41**(16), 7987–7996, DOI: 10.1093/nar/gkt575.

74 Y. Yuan, X. Zhao, S. Liu, Y. Li, Y. Shi, J. Yan and X. Hu, *Sens. Actuators, B*, 2016, **236**, 565–573, DOI: 10.1016/j.snb.2016.06.007.

75 Y. Gao, Y. Jiao, W. Lu, Y. Liu, H. Han, X. Gong and C. Dong, *J. Mater. Chem. B*, 2018, **6**(38), 6099–6107, DOI: 10.1039/C8TB01580E.

76 Y. Gao, H. Zhang, S. Shuang, H. Han and C. Dong, *Anal. Methods*, 2019, **11**(20), 2650–2657, DOI: 10.1039/C9AY00424F.

77 X. Liu, S. Zhang, H. Xu, R. Wang, L. Dong, S. Gao and A. Aldalbahi, *ACS Appl. Mater. Interfaces*, 2020, **12**(42), 47245–47255, DOI: 10.1021/acsami.0c12750.